Scientia Iranica B (2018) 25(5), 2693–2705

SCIENTIA IRANICA

Sharif University of Technology
Scientia Iranica
Transactions B: Mechanical Engineering
http://scientiairanica.sharif.edu

Atmospheric icing effects of S816 airfoil on a 600 kW wind turbine's performance

A. Ebrahimi[*]

Department of Aerospace Engineering, Sharif University of Technology, Tehran, P.O. Box 11155-1639, Iran.

Received 16 February 2017; received in revised form 9 June 2017; accepted 11 September 2017

KEYWORDS
Wind turbine;
Production loss;
Icing;
CFD;
BEM.

Abstract. This study investigates the aerodynamic loads and energy losses of a typical 600 kW wind turbine with S816 airfoil blade under two different icing conditions. Three sections at different radial positions were considered to estimate the icing effect along the blade. Ice accretion simulations in wet and dry regimes were carried out using the NASA LEWICE 3.2 computer program. The airflow simulations were performed with CFD method and SST $k-\omega$ turbulence model. The results of these simulations, including streamlines, surface pressure, skin friction, lift, and drag coefficients, were inspected for both clean and iced airfoils. In the case of wet iced airfoil, a separation bubble was created in the leading edge due to a horn-shaped ice and then further downstream, the airflow was reattached. Ice-induced separation bubbles dominate the flow field and aerodynamic performance of the wind turbine. In order to assess the production losses, the Blade Element Momentum (BEM) theory was used to calculate the power curves for clean and iced wind turbine blades. In the case of dry regime, deterioration of the performance is about 30% and, in another case, the turbine fails to produce any power at all.

1. Introduction

In terms of high wind speeds, many favorable sites for wind farms are located in cold, wet regions [1]. Cold regions with higher altitudes have usually higher wind speeds and, consequently, a significant potential for wind energy production. In addition, these areas are characterized by a potential for wind power, approximately 10% higher than other regions due to the presence of denser air at lower temperature [2]. However, such areas are inherently susceptible to atmospheric icing events during colder periods of the year. Icing can deteriorate the power production of a wind turbine severely by reshaping the blade airfoil [3]. This phenomenon deviates the aerodynamic performance significantly [4,5]. Icing effects are not limited to deterioration of blades' aerodynamic performance; also, they increase the dynamic loading and noise levels of wind turbines [6].

A considerable number of literature reviews on aircraft airfoil performance under icing condition are available; however, an equivalent database for wind turbine airfoils under atmospheric ground icing conditions hardly exists [7]. The assessment of performance losses on wind turbine blades due to ice accretion is a subject of particular interest to the wind turbine research community [8]. Both experimental and computational studies have been conducted to examine aerodynamic phenomena on iced airfoils and the effects of ice formation on deterioration of Horizontal Axis Wind Turbines' (HAWTs) performance. In the following, some of the most important ones are mentioned.

Bose [9] investigated the glaze ice formation on one blade of a small-scale HAWT. Bragg et al. [10] studied the time-averaged flow field and separation bubble formed around a glaze ice shape on a NACA

---

[*] *E-mail address: ebrahimi_a@sharif.ir*

doi: 10.24200/sci.2017.4521

0012 using split-film anemometry. Jasinski et al. [11] predicted the rime ice accretion on the S809 wind turbine airfoil using NASA LEWICE program. These data were used to estimate the effects of the rime ice on a 450 KW HAWT performance. Lee and Bragg [12] performed an experimental study to consider the aerodynamic effects of simulated large-droplet ice accretion on a modified NACA 23012 airfoil. Hochart et al. [13] experimentally studied the effects of glaze and rime ice formation on 1.8 MW-Vestas V80 wind turbine blade profile in a refrigerated wind tunnel. The resultant bending, driving forces, and torque distribution on rotors were computed by implementing the Blade Element Momentum (BEM) theory. Further, Homola et al. [14] studied the dependence of atmospheric icing on the temperature and wind turbine size by performing the numerical simulations of ice accumulation on five different wind turbine blade profiles at four different temperatures. Homola et al. [15] also carried out a numerical study of power performance losses due to the ice accretion on a large HAWT (NREL 5 MW) using CFD and BEM for rime ice conditions. Fu and Farzaneh [16] simulated the rimeice accretion process on a HAWT (NREL VI) operating under icing conditions based on a two-phase flow solution by means of a commercial CFD program.

Han et al. [7] performed the first experimental study about ice accretion on a rotating wind turbine blade. The numerical simulation over a clean and ice-accreted NACA 63-415 airfoil using commercial package FLUENT and SST $k-\omega$ turbulence model was conducted by Villalpando et al. [8]. Li et al. [6,17] also investigated the characteristics of surface icing on the wind turbine blades with the NACA0018 and NACA 7715 airfoils. Hudecz et al. [18] presented both experimental and numerical simulations of the effect of ice accretion on a NACA 64-618 airfoil. The effects of atmospheric icing on the loads and structural responses of a 5-MW land-based wind turbine were studied by Etemaddar et al. [19]. They used a commercial CFD program, FLUENT, to predict the aerodynamic coefficients of the blade after icing. The results were also validated against wind tunnel measurements using a NACA 64-618 airfoil. Lamraoui et al. [3] investigated the effects of atmospheric icing on V80-1.8 MW Vestas wind turbine. Jin et al. [20] experimentally studied the effects of a simulated single-horn glaze ice accreted on rotor blades on the vortex structures in the wake of a HAWT utilizing the stereoscopic particle image velocimetry (Stereo-PIV) technique. More recently, Ebrahimi et al. [21] experimentally investigated the upper and lower separation bubbles over a Natural Laminar Flow (NLF-0414) airfoil with double horn glaze ice geometry. In addition, Manshadi and Esfeh [22] studied the characteristics of the unsteady separation bubbles on a NACA 0015 airfoil with simulated two-dimensional leading-edge glaze ice accretions. Pedersen and Sørensen [23] developed a concept that unifies the ice accretion process and aerodynamic analysis into one CFD-based ice accretion model.

As presented, the aerodynamic performance of the various wind turbine airfoils under icing conditions has been investigated, while the NREL's S-series airfoils, widely used in wind turbine industries, have not been studied so far. In the present study, flow field characteristic over a S816 airfoil with and without simulated ice is investigated numerically. S816 is a thick-airfoil of NREL family that was specifically designed for large HAWTs in 1992. NREL S-series is a family of airfoils that were designed to be rather insensitive to roughness effects. Therefore, it is very important to investigate the deterioration of the performance of such an airfoil under icing conditions as a large-scale roughness.

2. Methodology

In the present research, two different atmospheric icing conditions are investigated to predict the level of wind turbine's performance deterioration due to the appearance of icing. First, different ice accretions caused by two different meteorological conditions on the wind turbine rotor blades in three blade cross-sections are simulated. Then, the aerodynamic properties of the iced airfoils for each case are modelled using CFD. Lastly, BEM calculations are used for the clean and iced wind turbine rotors to gain an insight into the consequences of icing conditions on the performance of a typical wind turbine. Figure 1 shows the procedure of this research.

3. Wind turbine blade

The implemented airfoil for simulating the shape of ice accretion is S816, which is a good approximation for

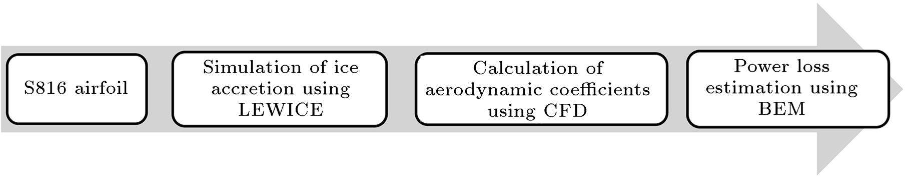

Figure 1. The procedure of this research.

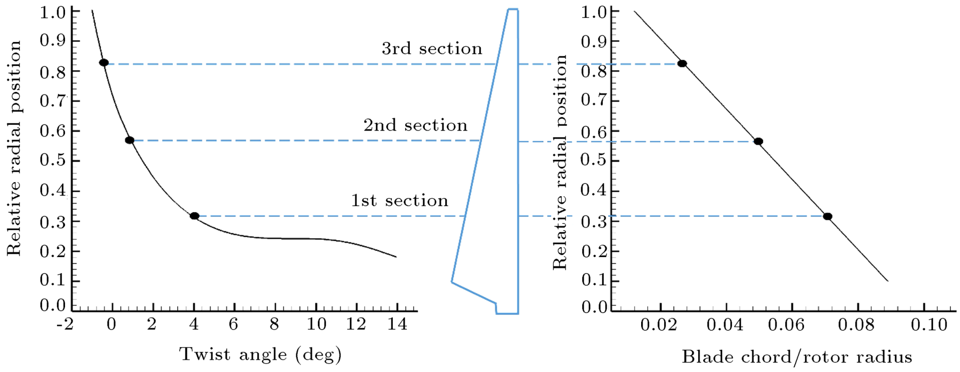

Figure 2. Pitch angle and chord length for selected blade airfoil sections.

typical airfoils employed in the rotor of 600 KW wind turbines. S816 is a thick laminar-flow airfoil of NREL airfoil family [24], specifically designed for 30 to 40-m diameters HAWTs in 1992. The primary design goals of this airfoil were to reach the maximum lift more gently, achieve insensitivity to roughness, and low profile drag [25]. Since ice accretion on blades depends on the relative velocity of the blade section, which changes with radial position, three sections located at different radial positions are chosen to study the deterioration of the blade performance. The radial positions, pitch angles, and chord lengths for selected airfoils along the turbine blade are illustrated in Figure 2. The rotor blade shown in this figure has been designed for a rated power of 600 kW under clean conditions. The numerical data is used in the BEM code to estimate the effects of the icing on the power production of a 47-m diameter three-blade rotor with a tip speed ratio of 7.

4. Numerical methods

4.1. Ice accretion model

Depending on the icing conditions, two distinct types of ice accretion (i.e., glaze and rime ice) may occur, although both usually occur within an icing accretion. Rime ice is associated with colder temperatures, lower Liquid Water Contents (LWC), and smaller Median Volumetric Diameters (MVD) compelling all the water collected in the impingement area to freeze on impact. Often, rime ice takes place on the original contour of the impingement area which is small and close to the leading edge. On the contrary, glaze ice is associated with warmer temperatures, higher LWC, and greater MVD causing only a fraction of the collected water to freeze in the impingement area; the remaining water runs back and may freeze outside the impingement area [26]. Generally, glaze ice introduces a more severe drag penalty than rime ice, since it creates an irregular airfoil surface and often has two protruded horns that considerably decrease the lift-to-drag ratio [7].

Herein, all the simulations of icing events are performed with the LEWICE software [27], developed by NASA Glenn Research Center. This solver employs the Messinger ice-accretion model [28] which provides results that are more accurate compared to other similar computational models' results, as demonstrated by Pallarol et al. [29]. Recently, Anttho and Sankar [30] implemented the extended Messinger model on wind turbine blades and validated the results using available 2D data.

4.2. Governing equations and airflow simulations

CFD simulations are conducted over 2D clean and iced S816 airfoils at various angles of attack. The results of surface pressure, skin friction, lift and drag coefficients for clean and iced airfoils are inspected. Simulations are performed with the commercial package ANSYS FLUENT 14.0 which is based on the finite-volume method. The two-dimensional Reynolds-Averaged Navier-Stokes (RANS) equations are implemented to simulate the incompressible flow (Mach number is lower than 0.1). The energy equation is not required to be solved. The continuity and momentum equations are presented as follows:

$$\frac{\partial \bar{u}_i}{\partial x_i}=0,$$

$$\frac{\partial \bar{u}_i}{\partial t}+\bar{u}_j\frac{\partial \bar{u}_i}{\partial x_j}=-\frac{1}{\rho}\frac{\partial \bar{p}}{\partial x_i}+\upsilon\frac{\partial^2 \bar{u}_i}{\partial x_j \partial x_j}+\frac{\partial \tau_{ij}}{\partial x_j}, \qquad (1)$$

where $\bar{u}_i$, $\bar{p}$, ρ, and υ are time-averaged velocity vector, time-averaged static pressure, density, and kinematic fluid viscosity, respectively. Reynolds stress tensor is defined by $\tau_{ij}=-\overline{u'_i u'_j}$.

Villalpando et al. [8] evaluated the efficiency of four turbulence models, i.e., Spalart Allmaras, SST $k-\omega$, RNG $k-\omega$, and RSM models, to estimate the aerodynamic coefficients. Among these turbulence models, SST $k-\omega$ model [31] shows good agreement with the experimental data and better performance in recirculation zones. Similar results have been found by Sagol et al. [32,33]. Since large recirculation zones are expected to appear over iced airfoil simulations, SST $k-\omega$ turbulence model is considered the best option for performing the simulations on the clean and iced airfoils in the present study. For the boundary conditions, the far field is set as pressure far field; the airfoil surface is set as wall (with no flow slip) and interior boundary conditions elsewhere. A pressure-based solver is employed with the SIMPLE algorithm for the pressure-velocity coupling. All of the variables are discretized with the second-order upwind scheme.

4.3. BEM calculations

The results of the aerodynamic force coefficients from the numerical simulation of airflow are used in the BEM program to estimate the effects of the icing on the power production of a 47-m diameter three-blade rotor. The power coefficient can be computed by integrating the torque acting into a finite number of discrete elements along the span of the blade. The differential torque (dQ) due to the tangential force (dF_T) acting on a single element of chord, c, at a radial position, r, on the blade (see Figure 3) can be computed by:

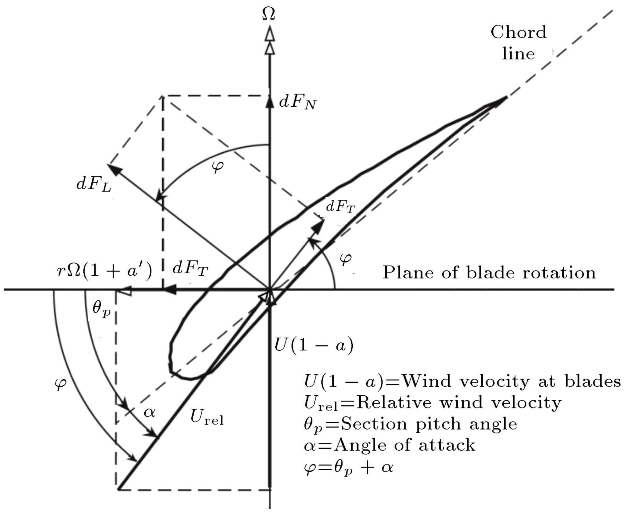

Figure 3. Forces (lift: d_{FL} and drag: d_{FD}), angles, and velocities at the blade section [34].

$$dQ = 0.5B\rho U_{\mathrm{rel}}^2 \left(C_\ell \sin\varphi - C_d \cos\varphi\right) crdr, \tag{2}$$

where B is the number of blades, U_{rel} is the sectional relative wind speed, and $\varphi = \theta_p + \alpha$ represents local blade inflow angle and is the sum of the section pitch angle (θ_p) and the angle of attack (α). The sectional airfoil lift and drag coefficients, C_ℓ and C_d, are functions of the angle of attack. The relative wind speed can be calculated by:

$$U_{\mathrm{rel}} = \sqrt{(U(1-a))^2 + (r\Omega(1+a'))^2}, \tag{3}$$

in which a and a' are the axial and angular induction factors, respectively. Given the wind speed, U, the rotor speed, Ω, and induction factors, the tangential force and rotor power can be calculated.

BEM theory has been developed to determine the performance of wind turbine blades by combining the equations of momentum theory and blade element theory. An iterative procedure is used for the solution to the BEM equations; for a given tip speed ratio, initial values for a and a' are assumed and used to calculate the inflow angle in the rotor plane. a and a' are presented as [34]:

$$a = \left\{1 + \frac{4F(\varphi)\sin^2\varphi}{\sigma C_\ell \cos\varphi}\right\}^{-1}, \tag{4}$$

$$a' = \left\{-1 + \frac{4F(\varphi)\cos\varphi}{\sigma C_\ell}\right\}^{-1}, \tag{5}$$

where $F(\varphi)$ is the Prandtl's tip-loss factor, and $\sigma = \frac{Bc}{2\pi r}$ is the local rotor solidity.

5. Validation of the simulations

Experimental data of [13] are used to validate the simulated ice shapes. Their study was carried out on a NACA 63-415 airfoil used as the 1.8 MW-Vestas wind turbine blade profile for three different radial positions and two icing conditions. Table 1 reports the wind tunnel parameters and atmospheric conditions under which the experiments are performed. In this table, r, α, V_∞, T_∞, and t refer to the radial position, angle of

Table 1. Characteristics of the icing events in the work by Hochart et al. [13].

Icing event	**Test**	r **(m)**	α **(°)**	V_∞ **(m/s)**	**LWC (g/m^3)**	T_∞ **(°C)**	t **(min)**
Wet regime	1	11.9	13	19.9	0.37	-1.4	14.8
	2	23.4	13	38.0	0.48	-1.4	15.1
	3	34.8	13	56.0	0.48	-1.4	24.8
Dry regime	4	11.8	3	18.7	0.37	-5.7	10.6
	5	23.3	7	36.7	0.48	-5.7	11.8
	6	35.0	9	55.0	0.48	-5.7	19.6

attack, air speed, air temperature, and time duration of the event, respectively. The MWD of the water droplets is 27.6 μm. According to the atmospheric conditions, tests 1 to 3 are in the wet regime, and tests 4 to 6 are in the dry regime. In the present study, the calculated shapes of the deposited ice for all simulations are compared with experimental results in Figure 4. The results of the deposited ice shape show acceptable agreement with the experimental data. Furthermore, experimental lift and drag coefficients of [13] for iced airfoils (Figure 4) are used to validate the CFD simulations. There is good agreement between the numerical results for the clean and iced airfoils along the blade radius and the experimental data, as shown in Figure 5.

6. Results and discussion

6.1. *Icing conditions and simulation of ice shapes*

In order to investigate the wind turbine performance under icing conditions, two icing events from a real wind farm [35,36] are selected for the simulations. The MVD and LWC for the wet regime are, respectively, 38.3 μm and 0.218 g/m^3, at -1.4°C and 360 seconds of event duration, while the MVD and LWC for the dry rgime are, respectively, 40.5 μm and 0.242 g/m^3, at -5.7°C and 264 seconds of event duration. These atmospheric conditions are applied to three different rotor blade cross-sections (airfoils with different chords, pitch angles, and relative wind speeds). The simulated

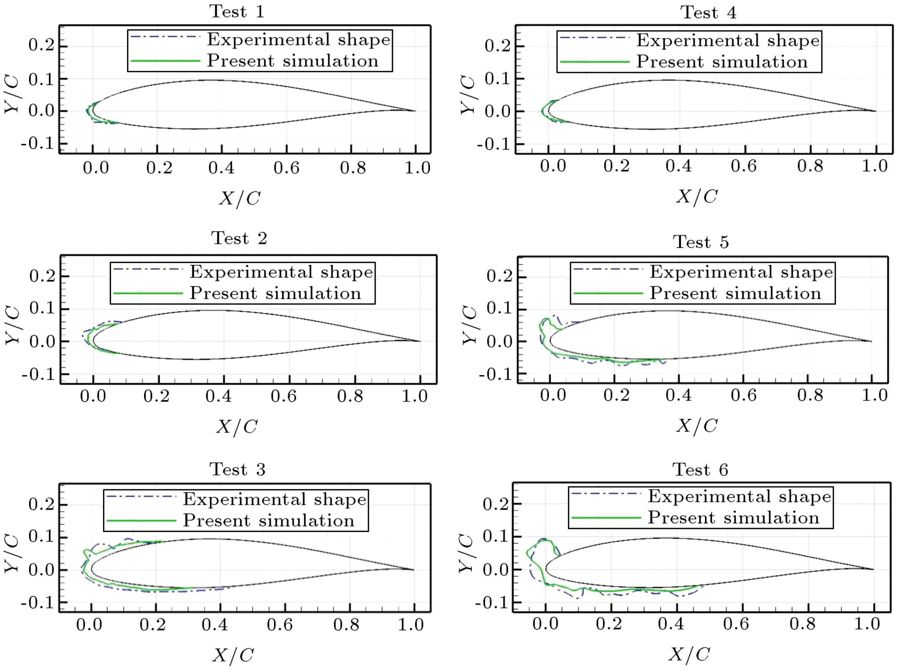

Figure 4. Calculated ice-deposit shapes compared with experimental results [13].

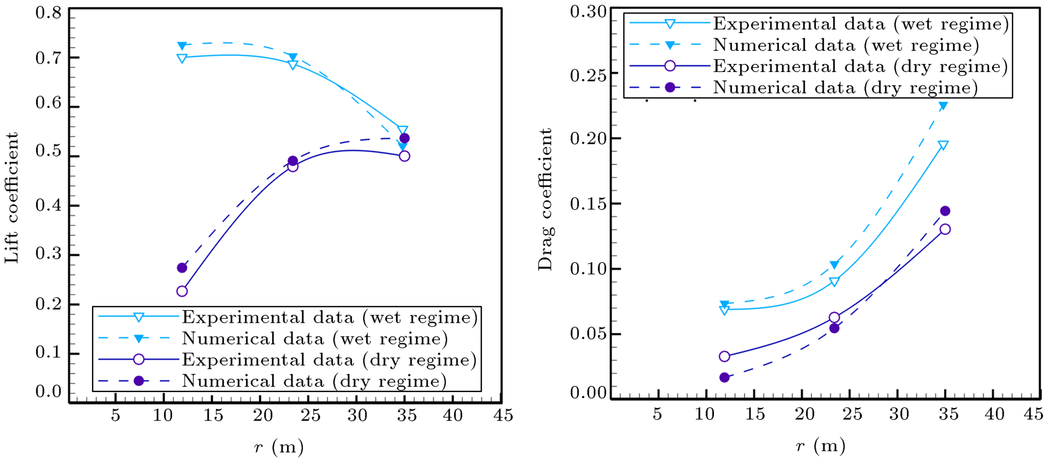

Figure 5. Comparison between the numerical and experimental [13] lift (a) and drag (b) coefficients along the blade radius for different icing events.

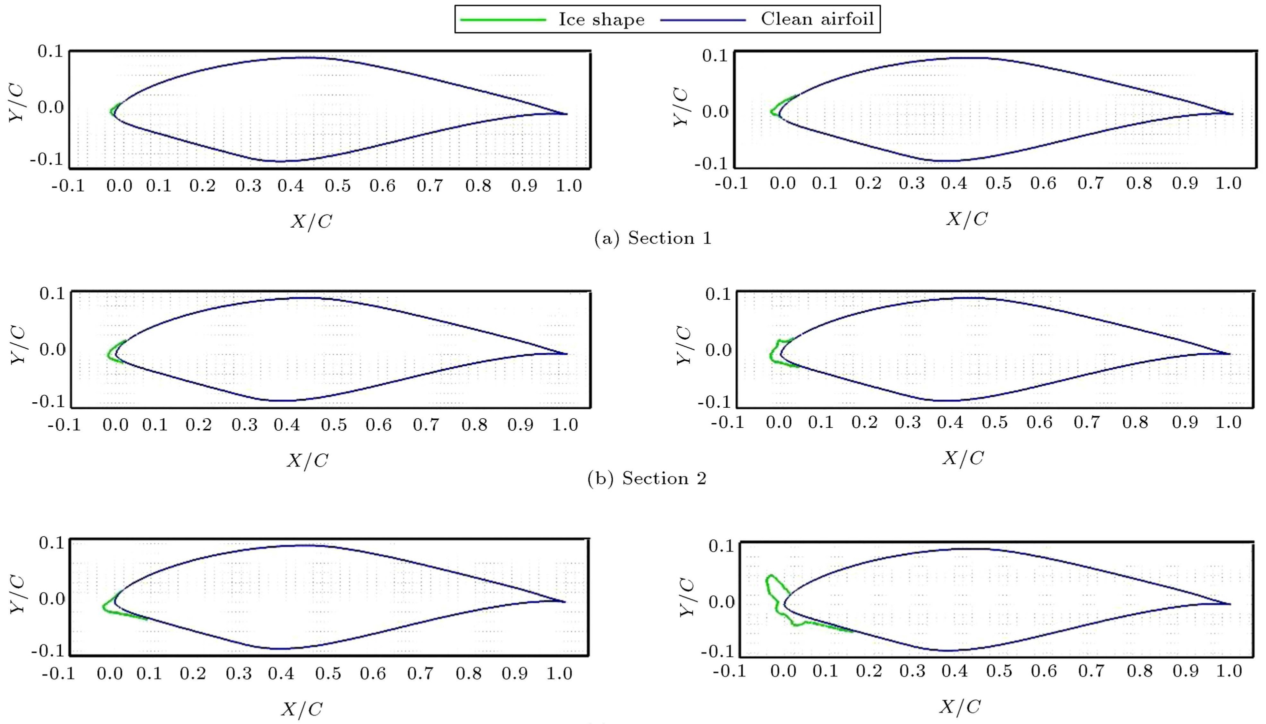

(a) Section 1

(b) Section 2

(c) Section 3

Figure 6. Simulated ice shapes on S816 airfoil in the dry regime icing (left) and in the wet regime icing (right).

ice profiles on S816 airfoil for various airflow speeds (9.2, 18.1, and 27.1 m/s) are illustrated in Figure 6 for the dry and wet regimes. The following points can be concluded:

1. In the wet and dry regimes, glaze ice and rime ice are mostly accreted on the leading edge;
2. Moving from the hub to the blade tip, ice accretion mass increases due to the increasing relative wind speed;
3. In the dry regime for Section 3, ice is formed mostly near the leading edge of the airfoil, whereas, in the wet regime, ice is accreted on the leading edge and partially on the pressure side of the blade section;
4. In the case of the dry regime, the ice mass collection distribution has a peak near the stagnation point and decreases to zero at the lower and upper surfaces; a similar trend was reported by Fortin and Perron [26].

6.2. Computational grid

A crucial step for analyzing the effects of icing on aerodynamic characteristics of airfoils is the generation of the computational grid for a complex ice shape. Vickerman et al. [37] developed a software toolkit, SmaggIce, for geometry grid generation in the presence of ice. Ice shapes have bumpy structures and are considered to feature large-scale surface roughness that must be treated as a part of the airfoil geometry. Herein, C-shape grids are generated and used in flow analyses for clean, simple rime and complex glaze ice shapes. A close-up near the leading edge of these grids is shown in Figure 7. The computational domain is extended 20 times the chord upward, downward, and upstream of the airfoil and 30 times the chord downstream of the airfoil. The quality of the cells remains satisfying while maintaining a minimum number of cells for optimizing the computational latency. Some features of the implemented grid and the convergence study are provided in Table 2. As the validity of

Table 2. Features of the implemented grid.

Number of cells	65,550	85,340	101,600	125,850
Averaged y^+	2.05	1.13	0.31	0.25
Maximum distance of wall from the first grid	8.36 e-3	3.52 e-3	1.21 e-3	1.01 e-3
Number of nodes in boundary layer	10	15	19	23
Area-weighted average of C_p	0.099	0.101	0.118	0.111
Error of C_p (%)	—	1.0	0.89	0.13

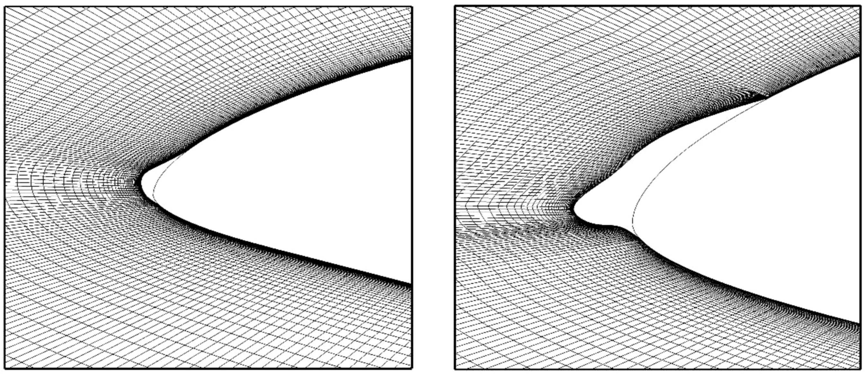

(a) Section 1

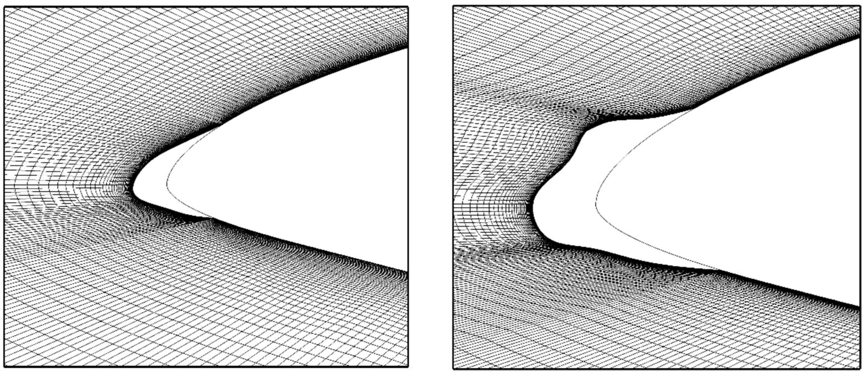

(b) Section 2

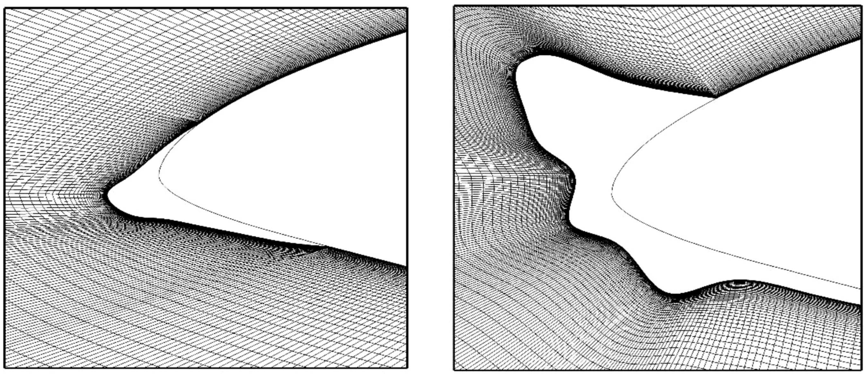

(c) Section 3

Figure 7. Generated grid in the dry regime icing (left) and in the wet regime icing (right) with a leading edge close-up.

turbulence models depends on the viscous length (y^+), averaged y^+ as well as the maximum distance of wall from the first grid and number of nodes in the viscous layer are also reported in Table 2. For grid convergence study, the area-weighted averages of pressure coefficient are calculated for the first section using a vertical line placed on 4% of chord downstream the trailing edge. The difference between the area-weighted averages of pressure coefficient of the present grid and the previous grid is also given in this table.

6.3. Flow field patterns

Figure 8 shows the comparisons of the streamlines around the clean and iced airfoils at three different angles of attack ($\alpha = 4°$, $6°$, and $8°$) and for Section 3 of the blade. In the case of the dry regime (Figure 8(d) and (e)), at low angles of attack (e.g., $\alpha = 4°$ and $6°$), the flow around the iced airfoil follows a pattern similar to the streamlines around the clean airfoil (Figure 8(a) and (b)); hence, it shows a low disturbance. In the case of the wet regime (Figure 8(g), (h), and (i)), the ice formations disturb most of the flow. The sharp edges at the suction side and large discontinuity in the surface geometry of the iced airfoil lead to acceleration of a flow speed, causing the boundary layer to be separated near the top of the horn ice shape; consequently, a separation bubble forms, as shown in Figure 8(g), (h), and (i).

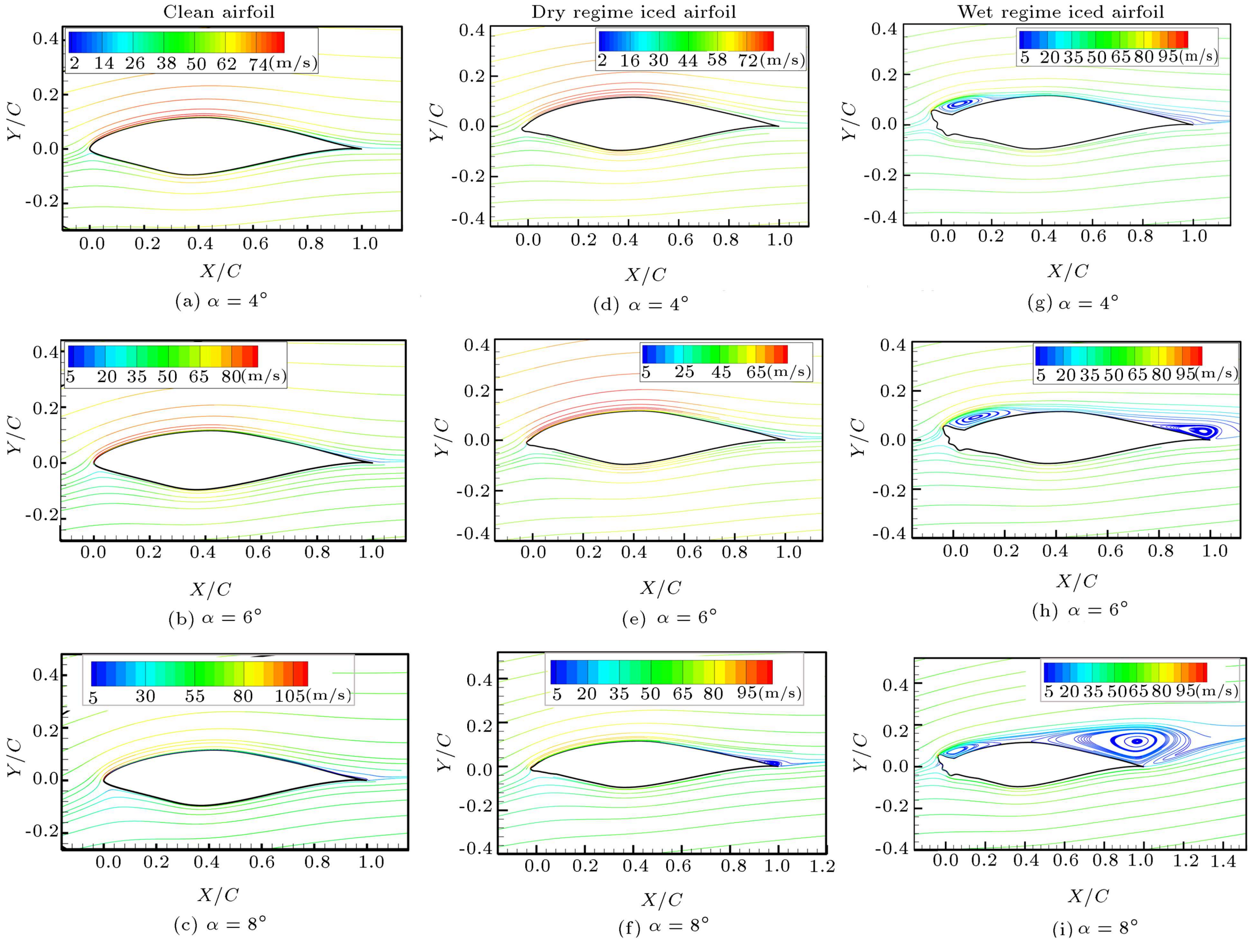

Figure 8. Streamlines (colored by velocity magnitude) for clean and different iced airfoil regimes for Section 3 of the blade.

6.4. Surface pressure and friction coefficients

Figure 9 depicts the comparisons of the surface pressure (C_p) and skin friction coefficients (C_f) along the clean and iced airfoils. Evaluation of the graphs in Figure 9 (left) illustrates that the surface pressure coefficient and, hence, the magnitude of the velocity in the dry regime, except near the leading edges, differ negligibly from the clean profile. While in the case of the wet regime (Figure 9-left), the separation bubble is the dominant flow feature that manipulates the surface pressure coefficient distribution and determines the aerodynamic forces. At the leading edge of the wet iced airfoil, pressure coefficient is seen to be nearly constant on the upper surface (e.g., Figure 9(a)). Since static pressure is fairly constant in a separation bubble [38], it can be concluded that the presence of separation bubble results in a constant pressure region at the leading edge.

The streamlines sketched in the wet regime (Figure 8(g), (h), and (i)) reveal that the boundary-layer separation point remains constant near the tip of the ice horn at all angles of attack. Near the horn, the pressure increases as the bubble starts to reattach. The plots of skin friction coefficients in Figure 9 (right) give insight into the bubble length. The Reattachment Point (RP) is located where the skin friction coefficient becomes zero, which is nearly equivalent to the inflection point of surface pressure coefficient curve, as shown in Figure 9 (left). Based on this criterion, the dimensionless locations of reattachment point of separated flow for various angles of attack are given in Table 3. As might be expected, the upper separation bubble is increased in size by increasing angle of attack (as seen in Figure 8(g) and (h)) to the point where the airflow of the upper surface separates completely (Figure 8(i)). About 30% of chord length is drowned by the largest calculated bubble at the angle of 6 degrees.

By increasing angle of attack to $\alpha = 8^\circ$ (and higher), a separation bubble forms at the trailing edge of the airfoil. This separated bubble overlaps with the leading edge separated bubble formed near the ice accretion; this phenomenon leads to the bubble bursting (i.e., the flow fails to reattach onto the airfoil surface). The airfoil stalls when the bubble bursts or fails to reattach. The tendency of the flow to form a long separation bubble and bubble bursting can lead to a significant loss in airfoil performance.

Figure 10 shows the streamlines and velocity

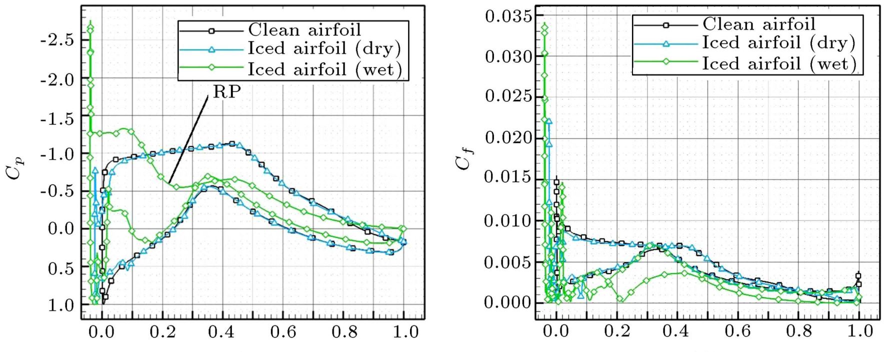

(a) $\alpha = 4°$

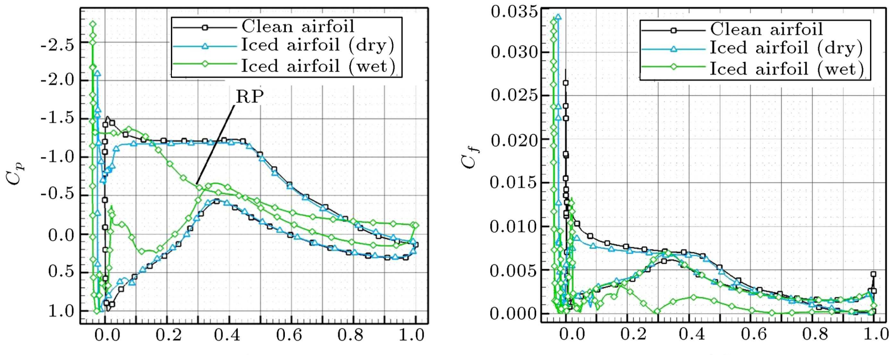

(b) $\alpha = 6°$

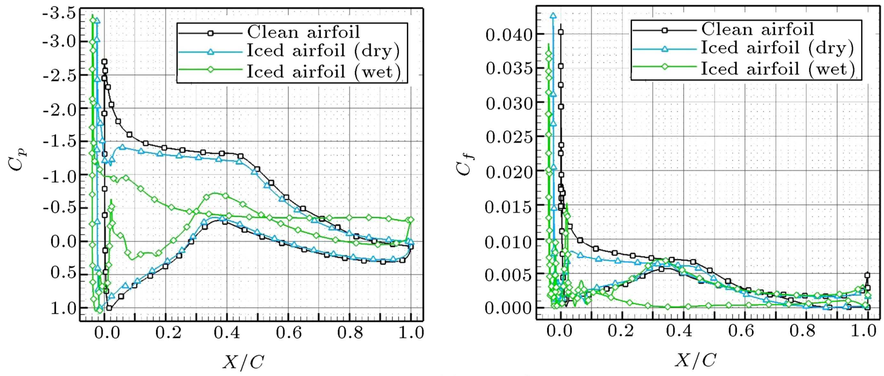

(c) $\alpha = 8°$

Figure 9. Surface pressure (left) and skin friction (right) coefficients for clean and different iced airfoil regimes for Section 3 of the blade.

Table 3. Bubble length and drag coefficients at different Angles Of Attack (AOA) in Section 3.

AOA (°)	**Bubble length in the wet regime** $\left(\frac{x}{c}\right)$	**Drag coefficient**				
		Clean profile	**Dry iced profile**	**Relative change (%)**	**Wet iced profile**	**Relative change (%)**
0	0.14	0.012	0.012	0	0.03	150
4	0.22	0.012	0.015	25	0.05	317
6	0.29	0.013	0.018	38	0.072	454

contours near the leading edge of the iced airfoil in the wet regime. As seen in this figure, at zero angle of attack, the leading-edge horn-ice shape leads to bubble formation on both upper and lower surfaces. In contrast to the upper surface separation bubble, the lower surface separation bubble decreases in size as the angle of attack increases. Moreover, as shown in this figure, the separation leads to the formation of a shear layer that separates the recirculation region from the high-speed inviscid flow above the bubble.

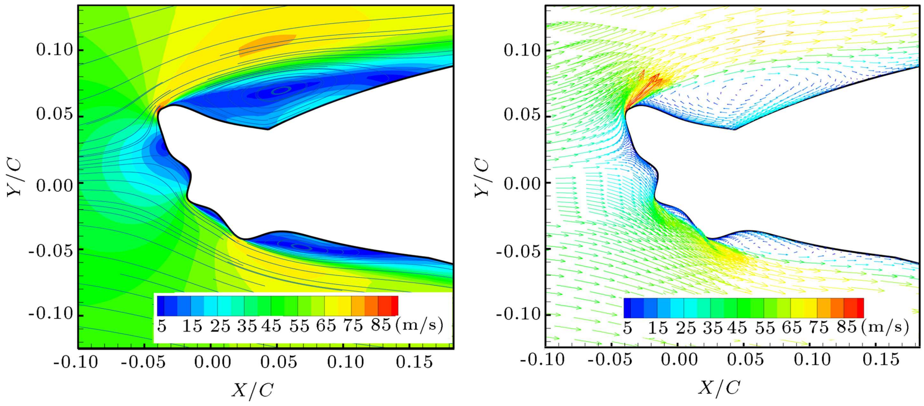

Figure 10. Velocity contours and streamlines in the wet regime at zero angle of attack.

6.5. Aerodynamic force coefficients

Main variables in the scope of this research are lift (C_ℓ) and drag coefficient (C_d). Lift and drag coefficients at three cross-sections of rotor blade are plotted for dry and wet ice conditions in Figures 11 and 12, versus angle of attack. Clean airfoil chord was used as the reference length for all the cases. Two most important features of the polars are the loss in maximum lift and the increase in drag as the degree of icing increases.

As seen in Figure 11, the ice shapes have a negligible effect on lift coefficient slope. In fact, the most significant difference is the decrease in maximum lift coefficient ($C_{\ell,\max}$) and stall angle (α_{stall}). The lift curves in Figure 11 show that the maximum lift is obtained for clean airfoil at $\alpha_{\text{stall}} = 20°$, for ice shape in the dry regime at the angle of about 10 degrees, and for ice shape in the wet regime at the angle of about 6 degrees. In the dry regime, the maximum lift coefficient decreases by 34.3% in Section 1, 7.6% in Section 2, and 27.8% in Section 3. In the wet regime, the maximum lift coefficient decreases by 34.3% in Section 1, 36.5% in Section 2, and 36.1% in Section 3.

As shown in Figure 11(c), another effect in Section 3 specific to the wet regime is the slight decrease of lift curve slope. Moreover, in this section, the separation bubble near the horn grows with the angle of attack and leads to thin-airfoil type stall. In this case, in contrast to the clean airfoil, the lift curve has a sharp peak in the vicinity of $C_{\ell,\max}$ followed by a rapid drop in lift coefficient at stall region.

In comparison with lift, the ice shapes have higher impact on drag coefficient, as demonstrated in Figure 12. Drag coefficient is multiplied owing to the ice geometry. Further, the drag increases continually from the hub to the tip. Figure 12(c) shows that the drag coefficient increment at the blade tip (Section 3) is estimated to be 515% at $\alpha = 8°$ in the wet regime and 25% at the same angle of attack in the dry regime. The sharp increment of drag in the wet regime is the consequence of bubble bursting.

As mentioned before, the wet regime iced airfoil has lost its basic aerodynamic shape at the leading edge (e.g., Figure 10), and a recirculation region has been generated right after the ice accumulation. The increase in bubble size and recirculation zone on the suction side of the airfoil results in a significant drag increment. In order to determine the importance of bubble length in predicting the drag, Table 3 shows the bubble length of the upper surface and drag coefficient versus the angle of attack for clean, dry and wet regimes of iced airfoil. In general, the wet regime introduces a worse drag penalty than the dry regime does, since it creates an irregular airfoil surface and often has two protruded horns that considerably decrease lift-to-drag ratio.

6.6. Power production loss

Figure 13 sketches BEM calculations for the output power of the 600 KW HAWT versus wind speed curve for icing of the three-bladed rotor in the clean and dry regime. Results show that the lift loss and drag increment for both icing conditions lead to a decrease in rotor torque. In the wet regime, due to the ice shape accreted on the blades, the drag force becomes too high compared to the lift, leading to the stoppage of the rotor rotating. The loss in performance due to icing in the dry regime is about 30% near the rated wind speed. Rime ice in the case of the dry regime is the usual deteriorating phenomenon during icing events in wind farms and is the main reason for production losses due to ice on wind turbines' blades.

7. Concluding remarks

The main purpose of the current study is to assess numerically the impact of ice accumulation on the blades of a 600KW HAWT with S816 airfoil sections under typical icing conditions. LEWICE was used to predict 2D ice profile shapes in the wet and dry regimes on the blade at three different span-wise locations. The results showed that due to the local relative velocity increment with the span, both mass and thickness of

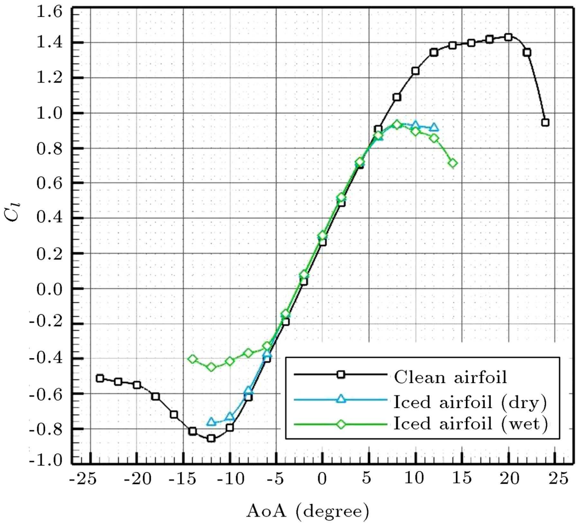

(a) Section 1

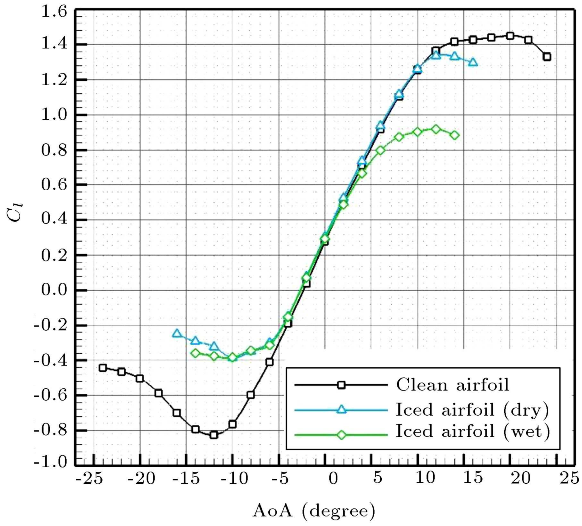

(b) Section 2

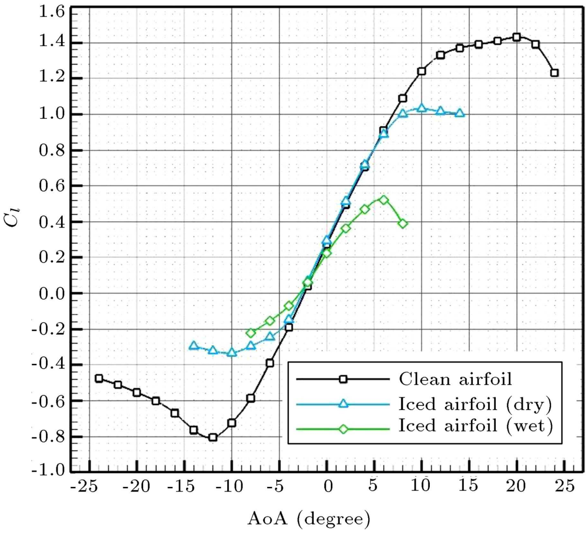

(c) Section 3

Figure 11. Lift coefficients for different regimes.

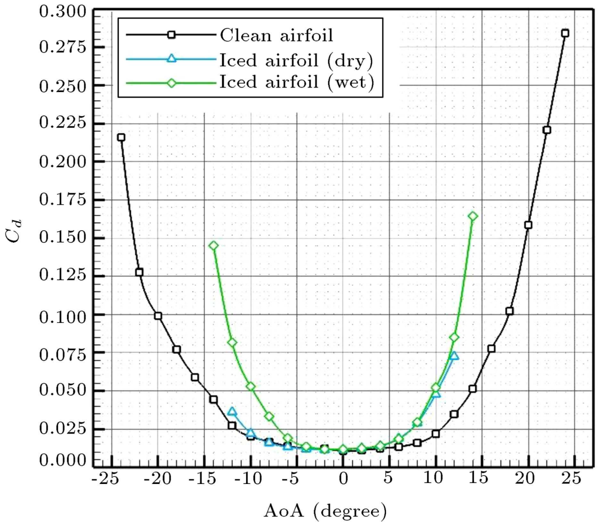

(a) Section 1

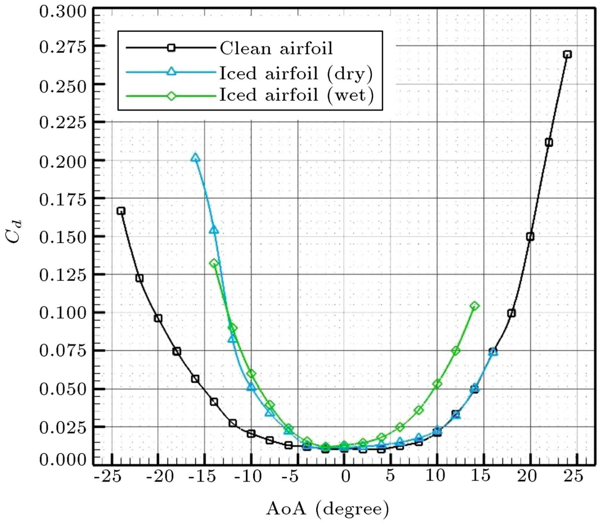

(b) Section 2

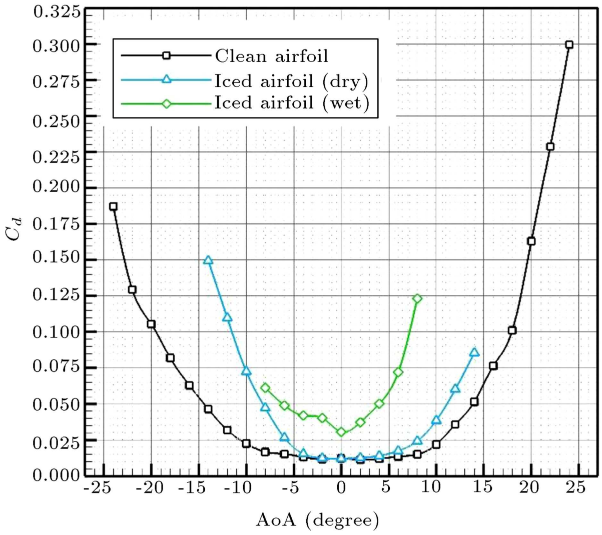

(c) Section 3

Figure 12. Drag coefficients for different regimes.

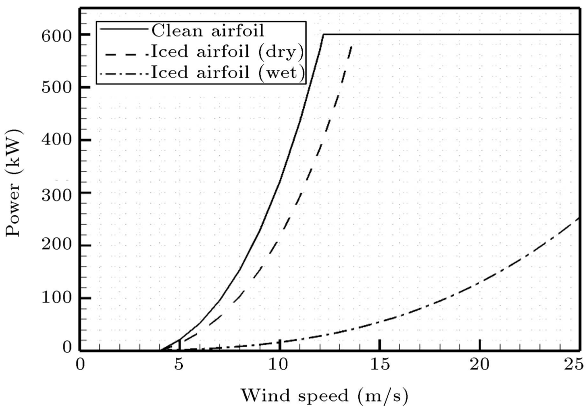

Figure 13. Power curves as a function of wind speed for clean and icing conditions.

accreted ice on the leading edge increase towards the blade tip. CFD analysis was performed to study the effect of the ice accretion on the airfoil aerodynamic performance at different angles of attack. The main findings can be summarized as follows:

1. In the dry regime, the accreted ice at the leading edge caused a small disturbance on the flow pattern, compared to the clean airfoil;
2. In the case of the wet regime, the horn-shaped ice led to the separation flow followed by a laminar separation bubble;
3. The separation region is usually recognizable on the C_p (surface pressure coefficient) plot by its almost constant value. The inflection point of chord-wise pressure distribution and zero skin friction were used as an indication of the reattachment point of the separation bubble;
4. Bubble length of the upper surface was estimated for different angles of attack in the wet regime of iced airfoil case. About 30% of chord length was drowned by the largest calculated bubble at the angle of 6 degrees;
5. The sharp increment of the drag force in the case of the wet regime (glaze iced-airfoil), at low angles of attack, was a result of the tendency of the flow to form a long separation bubble and, then, bubble bursting;
6. Analogous to other studies, lift and drag coefficients decreased and increased respectively as ice accreted. Deterioration of aerodynamic performance was more significant on the outer part of the blade;
7. In the wet regime, the maximum lift coefficient at the blade tip was found to reduce around 36%, and the drag coefficient was found to increase around 515% at $\alpha = 8°$ relative to the clean case at the blade tip;
8. In the dry regime, the maximum lift coefficient at the blade tip was reduced by an order of 28%, and the drag coefficient was increased by 25% at $\alpha = 8°$ relative to the clean case at the blade tip;
9. By means of BEM methods, power production losses of a 600 KW wind turbine due to iced rotor blade in the dry regime were estimated to be up to 30% near the rated wind speed. As shown, extreme changes in the airfoil performance in the wet regime conditions disrupted the power production procedure.

References

1. Barber, S., Wang, Y., Jafari, S., Chokani, N., and Abhari, R.S. "The impact of ice formation on wind turbine performance and aerodynamics", *Journal of Solar Energy Engineering*, **133**(1), pp. 1-9 (2011).
2. Fortin, G., Perron, J., and Ilinca, A. "A study of icing events at Murdochville: conclusions for the wind power industry", *International Symposium, Wind Energy in Remote Regions*, Maghdalen's Island, Canada (2005).
3. Lamraoui, F., Fortin, G., Benoit, R., Perron, J., and Masson, C. "Atmospheric icing impact on wind turbine production", *Cold Regions, Science and Technology*, **100**, pp. 36-49 (2014).
4. Dalili, N., Edrisy, A., and Carriveau, R. "A review of surface engineering issues critical to wind turbine performance", *Renewable and Sustainable Energy Reviews*, **13**(2), pp. 428-438 (2009).
5. Parent, O. and Ilinca, A. "Anti-icing and de-icing techniques for wind turbines: Critical review", *Cold Regions Science and Technology*, **65**(1), pp. 88-96 (2011).
6. Li, Y., Tagawa, K., Feng, F., Li, Q., and He, Q. "A wind tunnel experimental study of icing on wind turbine blade airfoil", *Energy Conversion and Management*, **85**, pp. 591-595 (2014).
7. Han, Y., Palacios, J., and Schmitz, S. "Scaled ice accretion experiments on a rotating wind turbine blade", *Journal of Wind Engineering and Industrial Aerodynamics*, **109**, pp. 55-67 (2012).
8. Villalpando, F., Reggio, M., and Ilinca, A. "Numerical study of flow around iced wind turbine airfoil", *Engineering Applications of Computational Fluid Mechanics*, **6**(1), pp. 39-45 (2012).
9. Bose, N. "Icing on a small horizontal-axis wind turbine - Part 1: Glaze ice profiles", *Journal of Wind Engineering and Industrial Aerodynamics*, **45**(1), pp. 75-85 (1992).
10. Bragg, M.B., Khodadoust, A., and Spring, S.A. "Measurements in a leading-edge separation bubble due to a simulated airfoil ice accretion", *AIAA Journal*, **30**(6), pp. 1462-1467 (1992).
11. Jasinski, W.J., Noe, S.C., Selig, M.S., and Bragg, M.B. "Wind turbine performance under icing conditions", *Journal of Solar Energy Engineering*, **120**, pp. 60-65 (1998).

12. Lee, S. and Bragg, M. "Experimental investigation of simulated large-droplet ice shapes on airfoil aerodynamics", *Journal of Aircraft*, **36**(5), pp. 844-850 (1999).
13. Hochart, C., Fortin, G., Perron, J., and Ilinca, A. "Wind turbine performance under icing conditions", *Wind Energy*, **11**(4), pp. 319-333 (2008).
14. Homola, M.C., Wallenius, T., Makkonen, L., Nicklasson, P.J., and Sundsbø, P.A. "Turbine size and temperature dependence of icing on wind turbine blades", *Wind Engineering*, **34**(6), pp. 615-28 (2010).
15. Homola, M.C., Virk, M.S., Nicklasson, P.J., and Sundsbø, P.A. "Performance losses due to ice accretion for a 5 MW wind turbine", *Wind Energy*, **15**(3), pp. 379-389 (2012).
16. Fu, P. and Farzaneh, M. "A CFD approach for modeling the rime-ice accretion process on a horizontal-axis wind turbine", *Journal of Wind Engineering and Industrial Aerodynamics*, **98**(4-5), pp. 181-188 (2010).
17. Li, Y., Chi, Y., Feng, F., Tagawa, K., and Tian, W. "Wind tunnel test on blade surface icing for vertical axis wind turbine", *Journal of Engineering Thermophysics*, **33**(11), pp. 1872-1875 (2012).
18. Hudecz, A., Koss, H., and Hansen, M. "Ice accretion on wind turbine blades", *15th International Workshop on Atmospheric Icing of Structures (IWAIS XV)* (2013).
19. Etemaddar, M., Hansen, M.O., and Moan, T. "Wind turbine aerodynamic response under atmospheric icing conditions", *Wind Energy*, **17**(2), pp. 241-265 (2014).
20. Jin, Z.Y., Dong, Q.T., and Yang, Z.G. "The effect of single-horn glaze ice on the vortex structures in the wake of a horizontal axis wind turbine", *Acta Mechanica Sinica*, **31**(1), pp. 62-72 (2015).
21. Ebrahimi, A., Hajipour, M., and Hasheminasab, H. "Experimental investigation on the aerodynamic performance of NLF-0414 iced-airfoil", *Journal of Applied Fluid Mechanics*, **9**(2), pp. 587-592 (2016).
22. Manshadi, M.D. and Esfeh, M.K. "Experimental investigation of flowfield over an iced aerofoil", *The Aeronautical Journal*, **120**(1227), pp. 735-756 (2016).
23. Pedersen, M.C. and Sϕrensen, H. "Towards a CFD model for prediction of wind turbine power losses due to icing in cold climate", In *16th International Symposium on Transport Phenomena and Dynamics of Rotating Machinery* (2016).
24. Tangler, J. and Somers, D., *NREL Airfoil Families for HAWTs*, National Renewable Energy Laboratory, NREL/TP-442-7109 (1995).
25. Somers, D.M., *The S816, S817, and S818 Airfoils*, National Renewable Energy Laboratory, NREL/SR-500-36333 (2004).
26. Fortin, G. and Perron, J. "Wind turbine icing and de-icing", AIAA 2009-274, Orlando, Florida: *47th AIAA Aerospace Sciences Meeting* (2009).
27. Wright, W.B., *User Manual for the Improved NASA Glenn Ice Accretion Code LEWICE*, National Aeronautical and Space Administration (NASA), CR-2002-211793 (2002).
28. Myers, G.T. "Extension to the Messinger model for aircraft icing", *AIAA Journal*, **39**(2), pp. 211-218 (2001).
29. Pallarol, J.G., Sunden, B., and Wu, Z. "On ice accretion for wind turbines and influence of some parameters", In *Aerodynamics of Wind Turbines: Emerging Topics*, Amano, R.S. and Sunden, B., pp. 129-160, WIT Press (2014).
30. Anttho, A.M. and Sankar, L.N. "In-cloud ice accretion modeling on wind turbine blades using an extended messinger model", In *13th International Energy Conversion Engineering Conference*, p. 3715 (2015).
31. Menter, F.R. "Zonal two-equations $k-\omega$ turbulence models for aerodynamic flows", AIAA Paper 93-2906, Orlando, FL; United States: *24th AIAA Fluid Dynamics Conference* (1993).
32. Sagol, E. "Three dimensional numerical prediction of icing related power and energy losses on a wind turbine", Doctoral dissertation, École Polytechnique de Montréal (2014).
33. Sagol, E., Reggio, M., and Ilinca, A. "Assessment of two-equation turbulence models and validation of the performance characteristics of an experimental wind turbine by CFD", *ISRN Mechanical Engineering*, **2012**, Article ID 428671 (2012). DOI: 10.5402/2012/428671
34. Manwell, J.F., McGowan, J.G. and Rogers, A.L., *Wind Energy Explained Theory, Design and Application*, 2nd Ed., Wiley (2010).
35. Mayer, C., Ilinca, A., Fortin, G., and Perron, J. "Wind tunnel study of electro-thermal de-icing of wind turbine blades", *International Journal of Offshore and Polar Engineering*, **17**(3), pp. 182-188 (2007).
36. Hochart, C., Fortin, G., Perron, J., and Ilinca, A. "Icing simulation of wind-turbine blades", AIAA 2007-1373, Reno, Nevada: *45th AIAA Aerospace Sciences Meeting and Exhibit* (2007).
37. Vickerman, M., Choo, Y., Schiling, H., et al. "Smaggice: further progress in software for gridding 2D iced airfoils", *AIAA Aerospace Sciences Meeting*, Reno NV.: AIAA Paper 2005-1369 (2005).
38. Katz, J. and Poltkin, A., *Low Speed Aerodynamics from Wing Theory to Panel Methods*, McGraw Hill (2001).

Biography

Abbas Ebrahimi received the PhD degree in Aerospace Engineering from the Sharif University of Technology, Tehran, Iran. He is currently an Associate Professor with the Aerospace Engineering Department of Sharif University of Technology. His research interests include wind turbines, CFD, applied aerodynamics, unsteady aerodynamics, and wind tunnel testing.